Volume 12 | Number 20 | 28 May 2016 | Pages 4501–4676

Soft Matter

www.softmatter.org

ISSN 1744-683X

ROYAL SOCIETY OF CHEMISTRY

PAPER
Abhishek Saha, Chao Sun *et al.*
Nonmonotonic response of drop impacting on liquid film: mechanism and scaling

Soft Matter

PAPER

View Article Online
View Journal | View Issue

Cite this: *Soft Matter*, 2016, 12, 4521

Nonmonotonic response of drop impacting on liquid film: mechanism and scaling

Xiaoyu Tang,[a] Abhishek Saha,*[a] Chung K. Law[ab] and Chao Sun*[bc]

Received 16th February 2016,
Accepted 4th March 2016

DOI: 10.1039/c6sm00397d

www.rsc.org/softmatter

Drop impacting on a liquid film with a finite thickness is omnipresent in nature and plays a critical role in numerous industrial processes. The impact can result in either bouncing or merging, which is mainly controlled by the impact inertia of the drop and film thickness. Although it is known that impact with inertia beyond a critical value on a thick film promotes merging through the breakage of the interfacial gas layer, here we demonstrate that for an impact inertia less than that critical value, increasing the film thickness leads to a nonmonotonic transition from merging to bouncing to merging and finally to bouncing again. For the first time, two different merging mechanisms are identified and the scaling laws of the nonmonotonic transitions are developed. These results provide important insights into the role of the film thickness in the impact dynamics, which is critical for optimizing operating conditions for spray or ink-jet systems among others.

1 Introduction

Drop impact on either liquid or solid surfaces is ubiquitous in many technological and natural processes affecting, for example, the quality of ink-jet printing through spreading and mixing of the inks,[1] the microstructure of thermal coatings,[2,3] the nature and extent of soot and pollutant formation through vaporization and subsequent burning of the liquid fuel spray deposited on engine surfaces,[4] and the erosion of soil and transport of the saline content through impacting rain drops.[5] Consequently, various fundamental aspects of drop impact have been extensively studied, including the effects of impact inertia, surface tension, and viscosity on outcomes such as the spreading,[6–10] splashing,[7,11–17] and bubble entrapment.[10,18–23] These outcomes, however, are largely conditioned on the coalescence of the impacting drop and the target surface, which may not always occur. Indeed, studies have shown that the impacting drop can bounce off the solid[24–27] or liquid[28,29] surfaces without coalescence. Thus, for a drop impacting on a surface, a central issue is whether the impact would lead to non-coalescence (bouncing) or coalescence (merging) of the drop with the surface, and the mechanism governing the transition from one to the other.

The dynamics of a drop impacting on a solid surface at which the drop deforms directly against the solid surface is characteristically different from that of a drop impacting on a liquid pool with a large thickness for which the deformation occurs at the pool surface and the base of the drop, and the effect of the solid surface below the liquid pool on the impact dynamics is minimal. For both cases, the impact inertia is the primary cause to break the interfacial gas layer instituting coalescence. However, much less studies have been conducted on the film thickness of the order of the drop size as both the drop and film deform through the influence of the solid surface under the liquid film, which subsequently affects the transition from bouncing to merging. Of particular interest is the observation of Pan *et al.*[29] that, while bouncing and merging respectively occur for small and large impact inertia, in the transition regime of the impact inertia, the impact outcome varies nonmonotonically with increasing film thickness. As the film thickness increases, the impact sequentially results in merging, bouncing, merging, and bouncing again. Using a different experimental setup, in the current work, we have reproduced this nonmonotonic behavior for larger drops and the outcome is summarized in Fig. 1. The new setup has the capability to provide detailed quantification of the impact dynamics beneath the liquid surface, which gives rise to further categorization of the merging regime into early and late merging, with the latter only appearing in the merging peninsula when H^* (defined as the film thickness normalized by the drop radius) is above 1.5. The existence and mechanistic difference between the two merging regimes are identified for the first time and the transition boundaries encompassing the late merging peninsula are analyzed and described using scaling laws. Furthermore, the transition criteria for other regimes are also systematically studied and established and the role of the bottom solid surface in the nonmonotonic transition is identified.

[a] *Department of Mechanical and Aerospace Engineering, Princeton University, Princeton, New Jersey 08544, USA. E-mail: asaha@princeton.edu*
[b] *Center for Combustion Energy, Tsinghua University, Beijing 100084, China. E-mail: chaosun@tsinghua.edu.cn*
[c] *Department of Thermal Engineering, Tsinghua University, Beijing 100084, China*

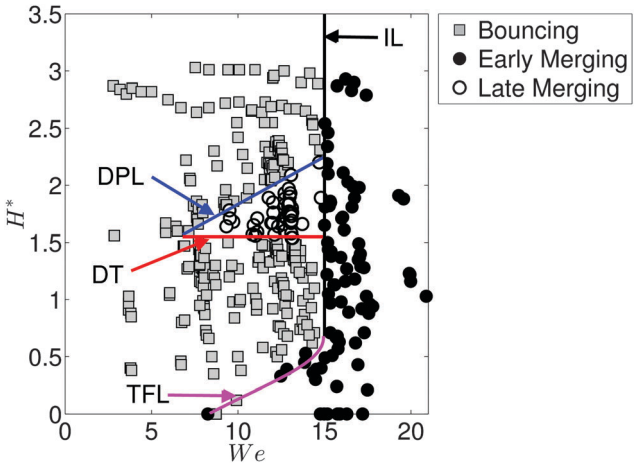

Fig. 1 Regime diagram of impact outcomes at various We = $2\rho RU^2/\sigma$ and film thicknesses normalized by drop radius $H^* = H/R$. Bouncing is represented by grey squares, while early and late merging are represented by the solid and open black circles, respectively. Transition boundaries across different regimes: IL: inertial limit; TFL: thin-film limit; DT: deformation transition; and DPL: deep-pool limit.

2 Method

The experimental setup (shown in Fig. 2) consists of a drop generator, two sets of high-speed cameras with appropriate lens systems and high-intensity light sources, and a timing unit to synchronize the cameras. The drop was generated by a syringe pump and it detached from the tip of the needle when its weight overcame the capillary force. The falling drop landed on the liquid pool contained in a cubic glass-walled chamber with a 1.2 mm thick microscope glass slide at the bottom. The width of the chamber was large enough to avoid the wall effects on the impact process. The drop generated was around 1.6 mm in diameter. The impact velocity of the drop was controlled by changing the height of the needle from the impacted surface. Tetradecane (density: 760 kg m^{-3}, air–liquid surface tension: 27 mN m^{-1}, and dynamic viscosity: 2.3 mPa s) was used as the working fluid.

A monochromatic high-speed camera (Phantom V7.3) along with a 50 mm lens (Nikon), a 2× tele-convertor and an extension bellow were placed to capture the side-view shadowgraph of the falling drop using a high intensity halogen light for backlighting. A separate high-speed color camera (Phantom V710) with a microscopic lens system (Navitar 6000) connected to a 5× objective (Mitutoyo) and a coaxially ported broadband white light (Olympus ILP2) was used to see through the glass surface at the bottom of the chamber to capture the interference pattern created by the thin interfacial gas layer trapped between the drop and film surfaces. The details of this technique of high-speed color interferometry are given in ref. 21 and 30. The interference pattern, which was observed until the interfaces merge, enabled an unambiguous identification of the merging instant. Both of these cameras were operated at 15 000 frames per second (fps), with spatial resolutions of ~17 μm and ~0.75 μm per pixel for side- and bottom-view images, respectively. The drop diameter, impact speed and liquid film thickness were measured by analyzing the side-view images from individual experiments. Images were post-processed using the commercial software MATLAB and its image-processing library.

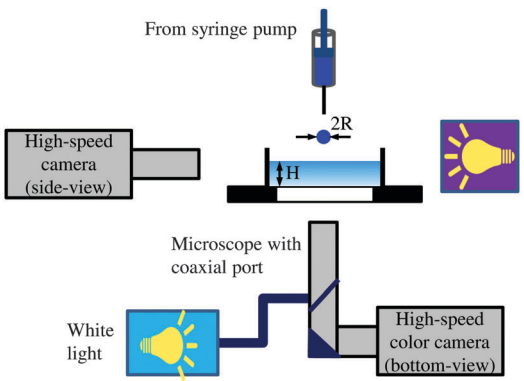

Fig. 2 Experimental setup.

3 Results and discussion

3.1 Regime diagram

Collision between two liquid masses can result in either merging or bouncing, in which the former is signified by the merging of the two interfaces while the latter by the separation of the interfaces throughout the entire impact event followed by bouncing. For droplet–droplet[31] and jet–jet[32,33] impacts the transition between different outcomes has been found to be nonmonotonic, changing from merging to bouncing to merging again with increasing impact inertia. These transitions have been explained through the competitive role of impact inertia, liquid deformation, internal viscous loss inside the liquid, and the pressure buildup in the interfacial region.[31,33] A drop impacting on a liquid surface likewise can also result in two outcomes: bouncing and merging. Mechanistically, as the drop approaches the stationary film, it deforms the liquid film and at the same time creates an interfacial gas layer which is squeezed by the inertia of the impacting drop. Under this squeezing motion, if the interfacial gas layer thickness is reduced to a critical value, typically of the order of a few hundred nanometers,[23,28,33,34] the intermolecular van der Waals force causes breakage of the gas layer and consequently merging of the two liquid surfaces. Such an impact is shown through a series of side-view high-speed images in Fig. 3a, where time t is the elapsed time after the drop reaches the liquid surface. As indicated in the first two frames in the figure, the interface between the deformed liquid pool surface and the drop separated by a gas layer can be visualized as a sharp "black" boundary. The drop starts penetrating the liquid pool upon impact, until the gas layer collapses at t = 3.66 ms, signified by the disappearance of the black boundary. On the other hand, if the interfacial gas layer remains thicker than a critical value, the drop and the liquid surfaces are separated throughout the entire penetration process. The film surface

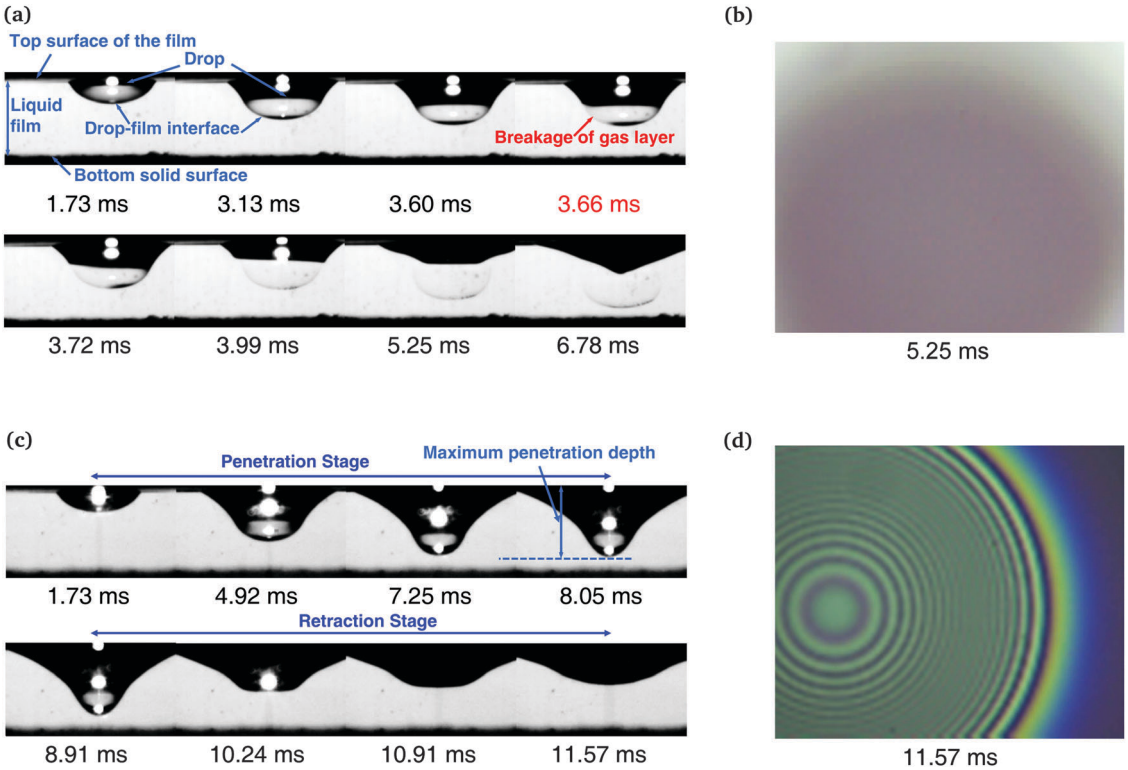

Fig. 3 Side-view (a and c) and bottom-view (b and d) snapshots of the drop-film impact event. (a and b) Merging case: We = 15.20 and H^* = 2.46. (c and d). Bouncing case: We = 11.98 and H^* = 2.55. Time is measured from the instant when the drop reaches the liquid surface.

and the drop start to retract at maximum deformation to regain their respective original spherical and planar shapes leading to bouncing. Fig. 3c shows the high-speed images of such a bouncing event: where one can identify the initial downward motion (penetration stage) followed by the upward motion of the film (retraction stage) while the boundaries indicating the interface are always present. The fact that the interfacial gas layer persists and separates the drop from the film is further supported by the continuous existence of the interference pattern resulting from the interfaces of the drop base and the liquid film surface, as shown in Fig. 3d. In the case of merging, however, the fringes disappear leaving a black zone in the bottom-view image in Fig. 3b, once merging occurs.

Mechanistically, the drop inertia and the surface deformation of the drop and liquid surfaces play critical roles in the impact dynamics, with the deformation controlled by the liquid surface tension and the liquid layer thickness. Consequently, the transition between bouncing and merging can be characterized by two nondimensional parameters: normalized film thickness, $H^* = H/R$, where H is the film thickness and R the drop radius, with the superscript "*" designating quantities normalized by the drop radius; and the Weber number, $We = 2\rho RU^2/\sigma$, which characterizes the ratio of drop inertia and surface tension. Here U, ρ, and σ are the drop impact velocity, the liquid density and the surface tension, respectively. The impact outcome in the H^*–We regime diagram is shown in Fig. 1 with the following characteristics. First, there is a critical Weber number, $We_{cr} \approx 15$, beyond which the drop always merges with the liquid film irrespective of its thickness. This boundary, referred to as the "inertial limit", is represented by the black solid line in Fig. 1. The "inertial limit" divides the regime diagram into a pure merging zone for higher We and a mixed zone of either merging or bouncing below We_{cr}, where the impact outcome varies nonmonotonically as H^* increases from 0, with transitions from merging to bouncing, to merging, and finally to bouncing again. This triple reversal of the impact outcome extends the merging zone near small H^* as a tail and near intermediate H^* as an additional merging peninsula. The first boundary at small film thickness ($H^* < 0.7$), where the transitional H^* shows a positive dependence on We, is termed the "thin-film limit", shown by the solid magenta line in Fig. 1. At the next transitional boundary (from bouncing to merging), which constitutes the bottom part of the merging peninsula, H^* does not show noticeable dependence on We, occurring at $H^* \approx 1.5$. We shall refer to this boundary as the "deformation transition", marked by the solid red line in Fig. 1. The final transitional line forms the upper boundary of the merging peninsula, where H^* increases with We, referred to as the "deep-pool limit", and is shown as the solid blue line in Fig. 1. We further divide the merging outcomes into two types, "early merging" and "late merging", which are respectively marked by solid and open black circles. The delineation of these sub-categories is discussed later.

3.2 Inertial limit

Mechanistically, when the drop impacts the liquid film with enough inertia, it can overcome the resistance due to the

pressure build-up in the interfacial gas layer, and locally succeeds in bringing the interfaces close enough for the van der Waals force to effect merging. The critical gas layer thickness d_{cr} for merging to occur is found to be around 200 nm.[23,28,33,34] A scaling dependence of the dimple height, a characteristic thickness of the gas layer, on the impact velocity for drop impact on solid surfaces has been derived and experimentally validated.[35,36] This dependence has been adopted successfully by Tran *et al.* for drops impacting on liquid pools.[21] According to this scaling, the dimple height of the air layer depends on the Stokes number, which corresponds to the relation, $d \sim U_p^{-2/3} R^{1/3} \rho^{-2/3} \mu_g^{2/3}$, where d is the dimple height, U_p the penetration velocity, which is the speed at which the drop moves into the liquid film, and μ_g the dynamic viscosity of the surrounding gas. The critical penetration velocity that reduces the gas layer thickness to the critical value d_{cr} is thus:

$$U_{p,cr} \sim \frac{\mu_g R^{1/2}}{\rho} d_{cr}^{-3/2} \quad (1)$$

It is noted that the process of merging through the collapsing gas layer is restricted to a localized zone around the interface and thus does not depend on the global parameters such as the liquid film thickness. However, the film thickness can alter U_p, which can be different from U. As the drop impacts the liquid film, it simultaneously deforms and pushes the liquid within the film, converting part of its kinetic energy to the surface and kinetic energies of the deformed film. The merging in this regime generally occurs very early in the penetration process, inhibiting significant deformation of the drop and the liquid film. Thus for simplicity we ignore the changes in the drop and liquid film surface energies. Viscous dissipation is also neglected in the present work because the Reynolds number is around 150. Moreover, Tran *et al.*[21] showed that the penetration processes for liquids with various viscosities indeed are very similar. To analyze the energy conversion, for the impact on a liquid film with a large thickness ($H^* > 1$), one can assume that the movement of the drop into the film generates a radial potential flow around the drop, as illustrated in Fig. 4a, where the flow velocity V in the film scales as $V \sim U_p R^3/r^3$, at distance r radially from the drop center. To evaluate the induced kinetic energy in the film with large thickness, KE_f, we integrate the kinetic energy of the infinitely thin shell with thickness dr at radius r, within the liquid film,

$$KE_f = \int_R^\infty 2\pi\rho r^2 V^2 dr \approx \int_R^\infty 2\pi\rho r^2 \left(U_p R^3/r^3\right)^2 dr = 2\pi\rho R^3 U_p^2 \quad (2)$$

Balancing the drop kinetic energy before the impact, $KE_{d,0} = 2\pi\rho R^3 U^2/3$, with the total kinetic energy of the drop, $KE_d = 2\pi\rho R^3 U_p^2/3$, and the film, $KE_f = 2\pi\rho R^3 U_p^2$, during the penetration process yields

$$U_p/U \approx 1/2 \quad (3)$$

Both in our experiments and the literature,[21] U_p is indeed found to be about half of U. It is also important to note that this relationship does not depend on H^* for large values of H^*.

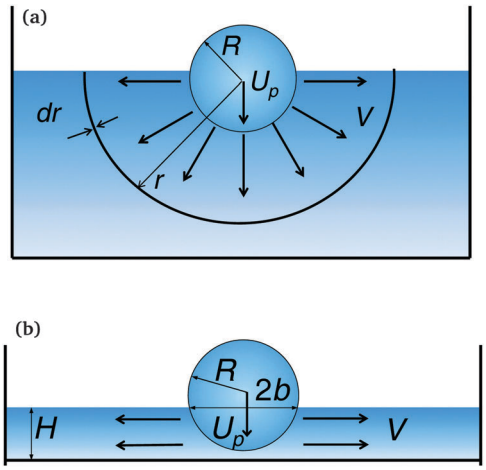

Fig. 4 Schematic of the flow field induced by the drop inside the liquid film: (a) inertial limit, (b) thin-film limit.

Combining eqn (1) and (3), we arrive at a critical impact velocity and the corresponding critical We, which is the measure of the minimum impact inertia required for merging, defining the inertial limit as

$$(U_{cr})_{IL} \sim \frac{2\mu_g R^{1/2}}{\rho} d_{cr}^{-3/2} \quad (4a)$$

$$(We_{cr})_{IL} \sim \frac{8\mu_g^2 R^2}{\rho\sigma} d_{cr}^{-3} \quad (4b)$$

It is seen that We_{cr} does not depend on the liquid film thickness and thus appears as a vertical line around 15 in the regime diagram (marked as the solid black line in Fig. 1). The transition from bouncing to merging across this limit is mainly controlled by the impact inertia.

For $We < We_{cr}$, the drop lacks sufficient impact inertia to break the interfacial gas layer and to induce merging. However, in the sub-critical regime there exist two extended merging sub-regimes, which are affected by the bottom solid surface, analyzed next.

3.3 Thin-film limit

As the film thickness is reduced to very small values, the penetration process is inhibited by the presence of the solid surface. This, in turn, modifies the flow field generated inside the liquid film. As shown in Fig. 4b, the motion inside the liquid film assumes a cylindrical rather than a spherical geometry as it is for large H^*. If we consider a liquid cylinder of radius b and height H that is displaced by the drop, the velocity of this displaced mass V is obtained by continuity $\rho\pi b^2 U_p \sim 2\rho\pi bHV$, where $b = R[H^*(2 - H^*)]^{1/2}$, the contact radius with the liquid film when the drop reaches the bottom, is found through the geometric consideration. The induced kinetic energy of this displaced mass, therefore, becomes $KE_f \sim \frac{1}{2}\pi\rho b^2 HV^2$. Following energy conservation before and

after the impact, we arrive at the relation $\frac{4}{3}\rho\pi R^3U^2 \sim \rho\pi b^2HV^2$. Thus the ratio of the impact and penetration We is

$$\frac{\mathrm{We}}{\mathrm{We_p}} = \frac{U^2}{U_p{}^2} \sim H^*(2-H^*)^2 \tag{5}$$

which increases as H^* increases.

Although the penetration velocity itself is affected by the film thickness, the critical value required for merging remains unaffected. The collapse of the gas layer is solely controlled by its local characteristic thickness; as such, eqn (1) is still relevant to calculate the critical penetration velocity. Eqn (1) and (5), therefore, determine $\mathrm{We_{cr}}$ for the thin-film limit as

$$(\mathrm{We_{cr}})_{\mathrm{TFL}} \sim \frac{2\mu_g{}^2R^2}{\rho\sigma} d_{\mathrm{cr}}{}^{-3}\left[H^*(2-H^*)^2\right] \tag{6}$$

which appears as a tail extension of the $\mathrm{We_{cr}}$ given by eqn (4b), into this regime with small H^* (shown as the solid magenta line in Fig. 1). As the film thickness increases within this regime, the drop is required to displace larger volume of liquid and hence transfers more energy to the film with less energy remaining to break the gas layer. Therefore, the impact requires a larger inertia or We for the transition to merging as indicated by eqn (6). As the film thickness further increases, the thin-film limit intersects with the inertial limit and the critical We is not dependent on H^* any more.

3.4 Deformation transition

When the film thickness increases to reach the deformation transition boundary, merging reappears. To compare the merging behavior of this regime with that beyond the inertial limit, the merging time, which is measured as the elapsed time between impacts, the time when the drop reaches the surface, and the breakage of the gas layer are examined for both the regimes. The histogram of the merging time (Fig. 5) displays a bi-modal distribution, in that the higher values (more than $\sim$8 ms) are only associated with impacts in this merging peninsula and all of the lower values (less than $\sim$5 ms) appear in the inertia-controlled merging regime beyond the inertial limit. The vastly distinguished merging times indicate the merging mechanisms

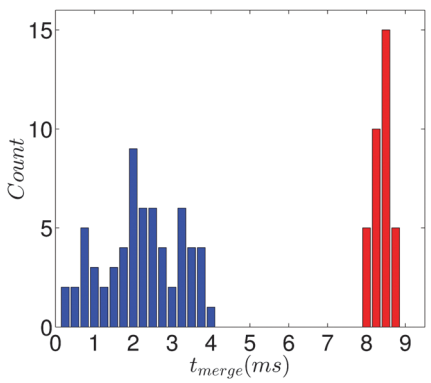

Fig. 5 Histogram of merging time. The merging time is calculated from the time the drop impacts on the surface to the instant the gas layer breaks. Blue: early merging; red: late merging.

are markedly different. We thus further categorize the merging regimes into late merging as occurring in this peninsula and early merging for the rest (Fig. 1).

To understand the cause of the late merging time in the peninsula, the side-view images of the bouncing and merging cases across the deformation transition are compared in Fig. 6. During the penetration process, although the actual drop is invisible in the side-view images, the shape of the liquid film can be a good indicator for the drop shape, as they closely follow each other near the bottom of the deformed film. From the bouncing case shown in Fig. 6a, as indicated by the variation of the width of the deformed film, one can readily see that upon reaching the bottom of the film, the drop deforms to spread along the solid surface, reaches a maximum width when it loses all the kinetic energy, and then retracts to bounce off. Careful observation of the high-speed images (Fig. 6b) of the merging case shows that it is during the retraction stage that the interfacial gas layer collapses, inducing merging. Unlike the early merging case where the gas layer collapses as the drop penetrates into the liquid film prior to reaching the bottom solid surface or maximum depth, for the late merging case, merging does not occur until the drop spreads on the bottom solid surface and starts to retract, leading to a longer merging time. It is not difficult to understand that for a fixed film thickness in the merging peninsula, increasing We from below to above the inertial limit leads to the change in the merging appearance from the retraction stage to the penetration stage. It is important to note that although the drop reaches close to the bottom surface and spreads, there always exists a very thin layer of liquid film between the drop and the solid surface. The complete depletion of the liquid film is extremely difficult for wettable solid surfaces and viscous liquids, such as the present one.

In order to scrutinize the dynamics of this transition from bouncing to merging, we first recognize that the drop behavior is analogous to a drop impacting on a dry surface,[7] where upon impact the drop deforms to a pancake shape and then to a vertical cylinder. The major difference, however, lies in the fact that for drop–film interactions, the film also spreads and retracts on the solid surface along with the drop. It is the competition between the retraction processes of these two surfaces that determines whether merging will occur. Categorically, if the film retracts faster than the deformed drop when both of them start to move up, it will catch up with the drop, inducing merging. The retraction speed is attained through the conversion from the excess surface energy. When the drop reaches the maximum spread, it loses all of its initial kinetic energy, with most of them converted to the additional surface energies of the deformed drop and film compared to the initial undisturbed state. As the surfaces relax during the retraction process, these additional surface energies are converted into the respective kinetic energies. At the point of maximum spread, if the additional surface energy contained in the deformed film is larger than that of the deformed drop, during the retraction process, the film will retract at a larger speed, facilitating merging.

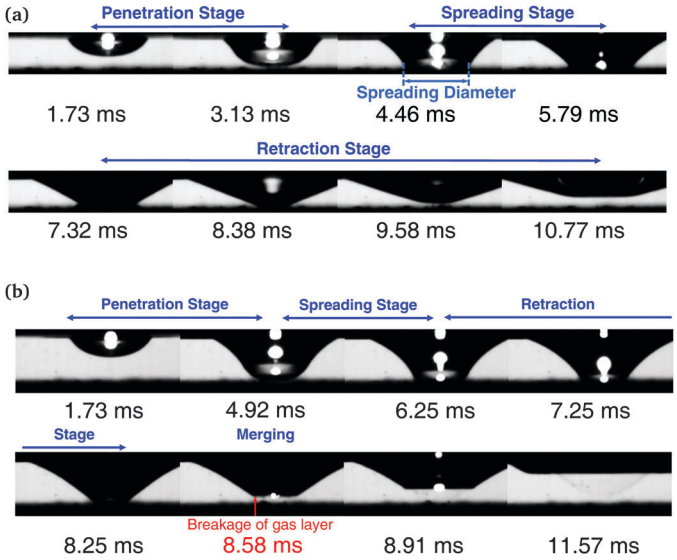

Fig. 6 Side-view snapshots near the lower boundary of the merging peninsula. (a) Bouncing case: We = 12.3 and H^* = 1.1. (b) Merging case: We = 12 and H^* = 1.67. Time is measured from the instant when the drop reaches the liquid surface.

To support the above argument that this particular transition from bouncing to merging is controlled by the relative deformation or the relative additional surface energies of the film and the drop, the ratio of these two quantities is plotted from the experiments in Fig. 7a. The additional film surface energy is directly calculated from the side-view images by multiplying the increase in the film surface area with surface tension, while the additional drop surface energy is calculated by subtracting the additional film surface energy from the initial kinetic energy of the drop. Fig. 7a clearly suggests that irrespective of We, the transition from bouncing to merging occurs when the ratio between the additional surface energies of the drop and the film crosses a certain limit. Thus the late merging is indeed facilitated by the bottom solid surface during the interaction between the drop and the liquid film, without any of which merging would not occur.

To analyze the relative deformation between the drop and the film as a function of the film thickness, we assume that at the point of maximum spread, the drop takes the shape of a short vertical cylinder, as shown in Fig. 7b. At this state, the increase in surface energies for the film and the drop can be expressed as $\Delta SE_f \approx \sigma(2\pi wH)$ and $\Delta SE_d \approx \sigma(2\pi w^2 + 2\pi wH_d) - \sigma(4\pi R^2)$, where H_d is the deformed drop height and $2w$ the maximum spread of the drop. By imposing the mass conservation between the undeformed and deformed drops, one can write $H_d = (4/3)R^3/w^2$. We can see that a larger film thickness allows more deformation in the film and thus a larger increase in the surface energy. In the limiting case, for merging to occur, the increase in surface energy of the deformed film equals to that of the drop, *i.e.* $\Delta SE_f \approx \Delta SE_d$. So for the transition we can write

$$H_{cr}^* \approx \left(w^* - \frac{2}{w^*} + \frac{4}{3}\frac{1}{w^{*2}}\right) \quad (7)$$

Eqn (7) suggests that the transition from bouncing to merging depends on $w^* = w/R$, which is the maximum radius of the deformed drop normalized by the drop radius. For drop

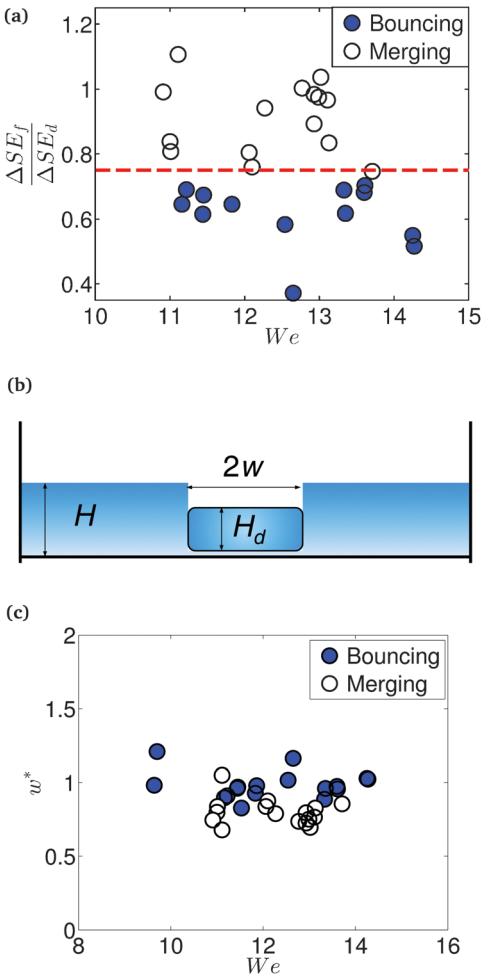

Fig. 7 Analysis of the deformation transition. (a) Ratio of the additional surface energies in the liquid film and the drop as a function of We. (b) Schematic of the simplified geometry when the drop reaches the bottom solid surface. (c) Normalized deformed drop radius as a function of We.

impacting on a solid surface, w^* is reported to have a weak dependence on We in the lower We region.[37–40] However, in the presence of the film, which significantly alters the spreading dynamics and limits the spreading of the drop, we find that w^* is practically independent of We in the limited We regime of the current work, as shown in Fig. 7c. This immediately suggests that the equation for the lower boundary of the merging peninsula is $H^* \approx$ constant, which takes a value of 1.5 for the current experiments, shown as the solid red line in Fig. 1.

3.5 Deep-pool limit

As the film thickness further increases, the next transition boundary is observed, as the impact results in bouncing again. Physically, for a fixed impact inertia, if the film thickness is beyond a certain value the penetration process will not be affected by the bottom surface anymore, reaching the deep-pool limit. Beyond this limit, even at the point of maximum penetration when the drop loses all its kinetic energy, it does not reach the bottom of the film. From experiments, as the drop moves through the film, we can track the distance between the original film surface and the bottom-most point of the drop, referred to as the penetration depth h_p. From the temporal evolution of the normalized penetration depth, h_p^* ($=h_p/R$), shown in Fig. 8a, we see that the drop penetrates into the film to reach a maximum depth before it starts moving upward. Comparing the different curves in Fig. 8a reveals that the maximum penetration depth increases with We. The maximum normalized penetration depth, $(h_p^*)_{max}$, across a range of We is plotted and found to roughly have a linear dependence on We, as shown in Fig. 8b. It is obvious that, unlike previous regimes, here the drop does not spread over the solid surface during the penetration process. With the absence of any aid for the deformation-induced merging, merging can only be instituted by the impact inertia, which is not large enough in this sub-critical region for $We < We_{cr}$, resulting in bouncing. Mechanistically, thus, the transition to this deep-pool regime from the merging peninsula occurs when $H^* > (h_p^*)_{max}$.

To identify the scaling dependence of $(h_p^*)_{max}$ on We, an energy analysis was performed assuming that all of the drop kinetic energy converts to the surface and kinetic energies of the liquid film when the drop reaches the maximum depth. Here, we neglect the drop deformation and consider the film deforms in the shape of a cylindrical well with a hemispherical cap, as shown in Fig. 8c. The kinetic energies for the drop and

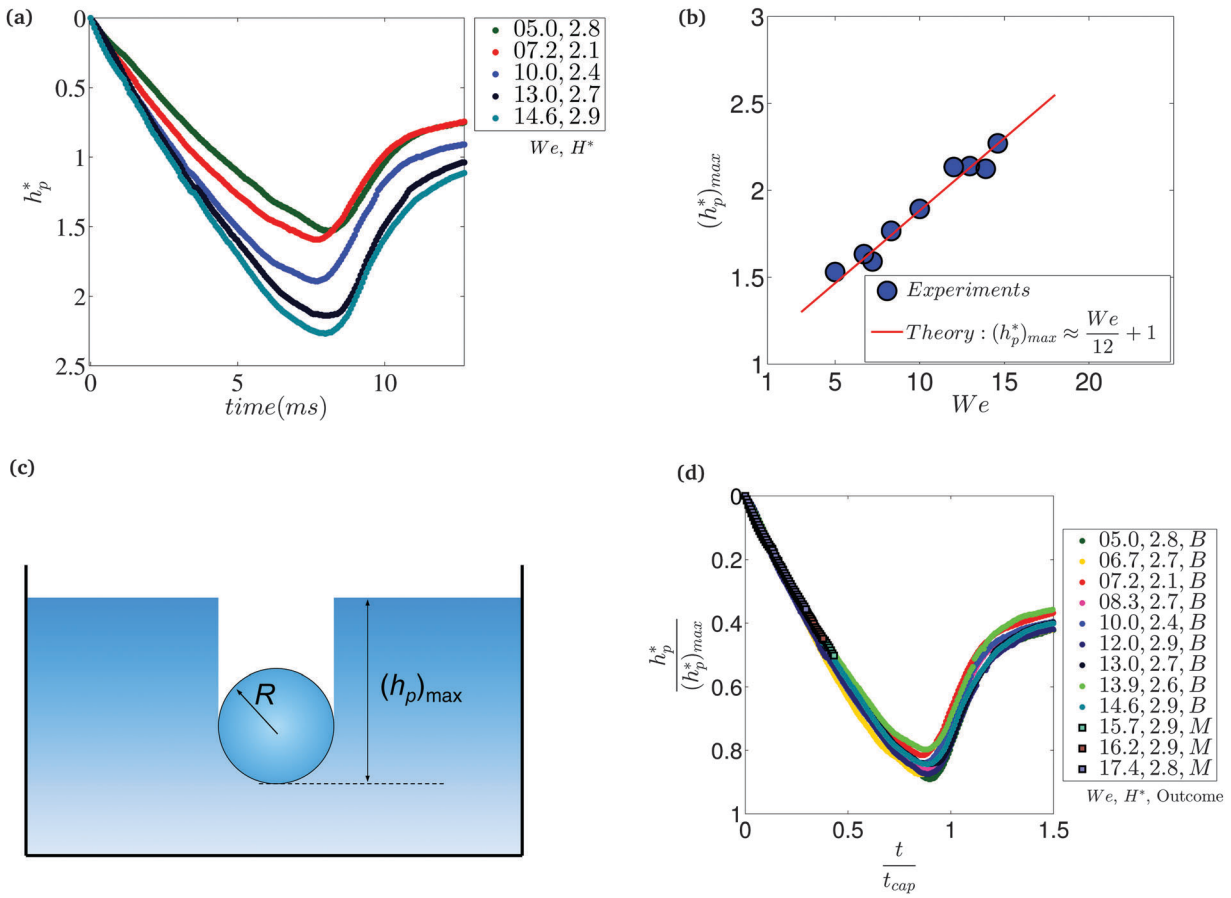

Fig. 8 Analysis of the deep-pool limit. (a) Time evolution of the penetration depth of drop normalized by drop radius for various We and H^*. (b) Maximum penetration depth *vs.* We. Solid circle: experiment; line: scaling. (c) Schematic of the simplified geometry at the maximum penetration. (d) Drop penetration depth normalized by the maximum penetration depth *vs.* time normalized by liquid film capillary time scale, $t_{cap} \approx 8.43$ ms for various We and H^*.

the film have already been modeled in eqn (2) and related discussions. The initial film surface energy is evaluated on a disc of radius R that is affected by the impacting drop to be $SE_{f,0} = \sigma\pi R^2$, while the film surface energy, when the drop reaches the maximum penetration, is $SE_f = \sigma[2\pi R((h_p)_{max} - R) + 2\pi R^2]$, based on the shape assumed. Balancing the total energy before the impact including the drop kinetic energy and film surface energy, $KE_{d,0}$ and $SE_{f,0}$, with the total energy when the drop reaches the maximum penetration including the kinetic energy of the film, KE_f, and surface energy of the film, SE_f, one finds that $(h_p^*)_{max}$ is linearly dependent on We, which can be expressed as $(h_p^*)_{max} = a + b\mathrm{We}$. The constants a and b are obtained from the best linear fit of the experimental data in Fig. 8b which results in $(h_p^*)_{max} \approx 1 + \mathrm{We}/12$. Finally, imposing the conditions that the transition from the merging peninsula to the deep-pool regime occurs when $H^* > (h_p^*)_{max}$, we can express the deep-pool limit (marked as the solid blue line in Fig. 1) as

$$H_{cr}^* \approx 1 + \mathrm{We}/12 \quad (8)$$

Two additional aspects of this limit are noted. First, as we have neglected gravity in the analysis, this scaling is valid only when the kinetic energy is much larger than the potential energy of the drop during the penetration process. In the regime studied, the gravitational effect is at most 5% of the kinetic energy ($U^2/gH \approx 24$). Extending eqn (8) to the limit of We $\to$ 0, thus, will not yield the correct penetration depth, as gravity will dominate the drop motion. Second, it is found that the time taken by the drop to reach the maximum penetration depth for all of the We in the deep-pool limit is almost identical, being about 8 ms, as seen in Fig. 8a. This is due to the fact that, in the sub-critical zone where We is low, the process is controlled by the capillarity of the film which is deformed to allow the drop to penetrate. The capillary time scale associated with the free surface is given by $t_{cap} = 2\pi/\omega_{cap}$, in which the angular speed can be expressed as $\omega_{cap} = (\sigma k^3 \tan(kH)/\rho)^{1/2}$, where k is the wavenumber of the disturbance.[41] For the drop impact in the deep-pool regime ($H \gg R$), one can approximate $k \approx 2/R$, resulting in $\tan(kH) \approx 1$. Thus, we can write $t_{cap} \approx 2\pi(\rho R^3/8\sigma)^{1/2}$, yielding $t_{cap} \approx 8.43$ ms, which is very close to the time taken by the drop to reach the maximum penetration depth. Now if the penetration traces are replotted using the experimental h_p^* normalized by the modeled $(h_p^*)_{max}$ given by eqn (8), and time t normalized by t_{cap}, one can collapse all the data for various We onto a master curve, as shown in Fig. 8d. Such a collapse of the temporal evolution of the drop motion confirms that the penetration process in this range of We is, indeed, mainly controlled by the liquid film capillarity.

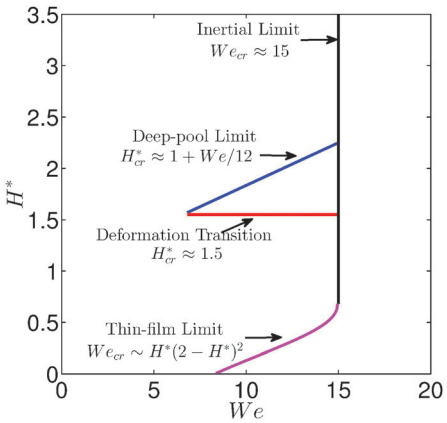

Fig. 9 Regime diagram with scaling laws for the transition boundaries.

4 Conclusion

We now summarize the bouncing–merging transitions for drops impacting on a liquid film at various We and H^*. In Fig. 9 we combine the scaling laws for all the transitional boundaries described through eqn (4b) and (6)–(8) on the regime diagram. The transition at the inertial limit occurs when a drop carries large enough inertia to break the interfacial gas layer inducing merging at the penetration stage. It is the penetration velocity that breaks the gas layer and is half of the impact velocity and independent of the film thickness for $H^* \gg 0$. Thus, the inertial limit, in essence, is a constant We line. However, when the film thickness reduces to small values, the bottom surface restricts the fluid motion in the film that modifies the flow field. With decreasing film thickness the drop loses less energy to the film, rendering merging easier. Thus, in the thin-film limit, We_{cr} decreases with decreasing H^*, forming a tail extension of the inertial limit. In the late merging peninsula, the gas layer is broken as the drop retracts against the bottom solid surface, contrasting that of the early merging case. A larger retraction speed of the film relative to the drop pushes the gas layer to collapse and is mainly controlled by the relative deformation. It is a function of the film thickness only, leading to a constant H_{cr}^* boundary for the deformation transition. Finally, the solid surface assisted merging disappears when the film thickness becomes too large for the drop to penetrate to the bottom. The maximum penetration depth of a drop linearly increases with the impact inertia and, as a result, H_{cr}^* shows a linear dependence on We at the deep-pool limit.

Acknowledgements

The work at Princeton University was supported in part by Xerox Corporation and by the Combustion Energy Frontier Research Center, an Energy Frontier Research Center funded by the U.S. Department of Energy, Office of Basic Energy Sciences under Award Number DESC0001198. The authors thank Roeland van der Veen of the University of Twente for helpful discussions on high-speed interferometry.

References

1 B. Samuel, H. Zhao and K.-Y. Law, *J. Phys. Chem. C*, 2011, **115**, 14852–14861.
2 S. Chandra and C. T. Avedisian, *Proc. R. Soc. A*, 1991, **432**, 13–41.

3 M. Pasandideh-Fard, V. Pershin, S. Chandra and J. Mostaghimi, *J. Therm. Spray Technol.*, 2002, **11**, 206–217.
4 R. D. Reitz, *Combust. Flame*, 2013, **160**, 1–8.
5 Y. S. Joung and C. R. Buie, *Nat. Commun.*, 2015, **6**, 6083.
6 A. Worthington, *Proc. R. Soc. A*, 1876, **25**, 261–272.
7 A. Yarin, *Annu. Rev. Fluid Mech.*, 2006, **38**, 159–192.
8 J. Eggers, M. A. Fontelos, C. Josserand and S. Zaleski, *Phys. Fluids*, 2010, **22**, 062101.
9 S. Jung and I. M. Hutchings, *Soft Matter*, 2012, **8**, 2686–2696.
10 C. Josserand and S. Thoroddsen, *Annu. Rev. Fluid Mech.*, 2016, **48**, 365–391.
11 M. Mani, S. Mandre and M. P. Brenner, *J. Fluid Mech.*, 2010, **647**, 163–185.
12 S. Mandre and M. P. Brenner, *J. Fluid Mech.*, 2012, **690**, 148–172.
13 L. Xu, W. W. Zhang and S. R. Nagel, *Phys. Rev. Lett.*, 2005, **94**, 184505.
14 S. Thoroddsen, *J. Fluid Mech.*, 2002, **451**, 373–381.
15 R. Krechetnikov and G. M. Homsy, *J. Colloid Interface Sci.*, 2009, **331**, 555–559.
16 L. V. Zhang, P. Brunet, J. Eggers and R. D. Deegan, *Phys. Fluids*, 2010, **22**, 122105.
17 L. Zhang, J. Toole, K. Fezzaa and R. Deegan, *J. Fluid Mech.*, 2012, **690**, 5–15.
18 L. Esmailizadeh and R. Mesler, *J. Colloid Interface Sci.*, 1986, **110**, 561–574.
19 H. N. Oguz and A. Prosperetti, *J. Fluid Mech.*, 1990, **219**, 143–179.
20 H. C. Pumphrey and P. A. Elmore, *J. Fluid Mech.*, 1990, **220**, 539–567.
21 T. Tran, H. de Maleprade, C. Sun and D. Lohse, *J. Fluid Mech.*, 2013, **726**, R3.
22 S. Thoroddsen, T. Etoh and K. Takehara, *J. Fluid Mech.*, 2003, **478**, 125–134.
23 S. Thoroddsen, M.-J. Thoraval, K. Takehara and T. Etoh, *J. Fluid Mech.*, 2012, **708**, 469–479.
24 G. P. Neitzel and P. Dell'Aversana, *Annu. Rev. Fluid Mech.*, 2002, **34**, 267–289.
25 D. Richard, C. Clanet and D. Quéré, *Nature*, 2002, **417**, 811.
26 J. de Ruiter, R. Lagraauw, D. van den Ende and F. Mugele, *Nat. Phys.*, 2015, **11**, 48–53.
27 J. Kolinski, L. Mahadevan and S. Rubinstein, *Europhys. Lett.*, 2014, **108**, 24001.
28 Y. Couder, E. Fort, C.-H. Gautier and A. Boudaoud, *Phys. Rev. Lett.*, 2005, **94**, 177801.
29 K.-L. Pan and C. K. Law, *J. Fluid Mech.*, 2007, **587**, 1–22.
30 R. C. van der Veen, T. Tran, D. Lohse and C. Sun, *Phys. Rev. E: Stat., Nonlinear, Soft Matter Phys.*, 2012, **85**, 026315.
31 J. Qian and C. Law, *J. Fluid Mech.*, 1997, **331**, 59–80.
32 N. Wadhwa, P. Vlachos and S. Jung, *Phys. Rev. Lett.*, 2013, **110**, 124502.
33 M. Li, A. Saha, D. Zhu, C. Sun and C. K. Law, *Phys. Rev. E: Stat., Nonlinear, Soft Matter Phys.*, 2015, **92**, 023024.
34 P. D. Hicks and R. Purvis, *Phys. Fluids*, 2011, **23**, 062104.
35 W. Bouwhuis, R. C. A. van der Veen, T. Tran, D. L. Keij, K. G. Winkels, I. R. Peters, D. van der Meer, C. Sun, J. H. Snoeijer and D. Lohse, *Phys. Rev. Lett.*, 2012, **109**, 264501.
36 E. Klaseboer, R. Manica and D. Y. Chan, *Phys. Rev. Lett.*, 2014, **113**, 194501.
37 C. Clanet, C. Béguin, D. Richard and D. Quéré, *J. Fluid Mech.*, 2004, **517**, 199–208.
38 C. W. Visser, P. E. Frommhold, S. Wildeman, R. Mettin, D. Lohse and C. Sun, *Soft Matter*, 2015, **11**, 1708–1722.
39 H. Lastakowski, F. Boyer, A.-L. Biance, C. Pirat and C. Ybert, *J. Fluid Mech.*, 2014, **747**, 103–118.
40 J. Lee, N. Laan, K. de Bruin, G. Skantzaris, N. Shahidzadeh, D. Derome, J. Carmeliet and D. Bonn, *J. Fluid Mech.*, 2015, **786**, R4.
41 E. Lifshitz and L. Landau, *Course of Theoretical Physics*, Fluid Mechanics, 1959, vol. 6.